

Observation of Ultra-low AC Susceptibility in Micro-magnets Using Quantum Diamond Microscope

Dasika Shishir,¹ Matthew L. Markham,² and Kasturi Saha^{1,3,4,*}

¹*Department of Electrical Engineering, Indian Institute of Technology Bombay, Mumbai, Maharashtra, India[†]*

²*Element Six, Harwell OX11 0QR, United Kingdom*

³*Center of Excellence in Quantum Information, Computing Science and Technology, Indian Institute of Technology Bombay, Powai, Mumbai-400076, India*

⁴*Center of Excellence in Semiconductor Technologies (SemiX), Indian Institute of Technology Bombay, Powai, Mumbai-400076, India*

AC susceptometry, unlike static susceptometry, offers a deeper insight into magnetic materials. By employing AC susceptibility measurements, one can glean into crucial details regarding magnetic dynamics. Nevertheless, traditional AC susceptometers are constrained to measuring changes in magnetic moments within the range of a few nano-joules per tesla. Additionally, their spatial resolution is severely limited, confining their application to bulk samples only. In this study, we introduce the utilization of a Nitrogen Vacancy (NV) center-based quantum diamond microscope for mapping the AC susceptibility of micron-scale ferromagnetic specimens. By employing coherent pulse sequences, we extract both magnitude and the phase of the field from samples within a field of view spanning 70 micro-meters while achieving a resolution of 1 micro-meter. Furthermore, we quantify changes in dipole moment on the order of a femto-joules per tesla induced by excitations at frequencies reaching several hundred kilohertz.

I. INTRODUCTION

Micro and nano-scale magnetic materials play crucial role across a spectrum of scientific, industrial, and research domains. Recent advancements have underscored their significance in diverse applications, such as utilizing magnetic states in micro-magnets for memory storage [1, 2], employing magnetic nanoparticle-based biomedicine [3], exploring biosensing capabilities [4], investigating exotic quantum phases like the quantum spin Hall effect, spin liquids [5], and pioneering spin-based computing [6]. Central to understanding these materials is the magnetic susceptibility, a pivotal parameter characterizing their magnetic properties. Particularly, the measurement of AC susceptibility [7] offers insights into ferromagnetic dynamics, including domain wall velocity and vortex motion [7, 8]. However, conventional tools for assessing AC susceptibility are limited, typically detecting changes in magnetic moments of just a few nJ T^{-1} [8, 9]. To contextualize this quantity, consider that the magnetic moment of a saturated cast iron cube—measuring approximately $11\ \mu\text{m}$ per side, with a saturation magnetization of $8 \times 10^5\ \text{A m}^{-1}$ is around $1\ \text{nJ T}^{-1}$. Remarkably, in a thin film of iron with the same lateral dimensions but a thickness of about 10 nanometers, the magnetic moment decreases to a mere $1\ \text{pJ T}^{-1}$. Under unsaturated conditions, magnetic moments can even be of the order of $1\ \text{fJ T}^{-1}$.

In recent years, there has been a surge in the characterization of magnetic materials at the nanoscale, facilitated by the remarkable magnetic field sensing capabilities of negatively charged nitrogen vacancy centers in diamond (NV^- centers in diamond). This advancement has enabled the characterization of a broad range of materials, including conventional ferromagnets [10–14], 2D van der Waals magnets [15–21], and magnetic particles found in biological systems [22–24]. Most

studies in this realm have focused on measuring the static or DC magnetic susceptibility, typically achieved by gauging the stray magnetic field emitted by the material under various external magnetic field conditions. Notably, in many instances, the magnitude of the stray field from the sample is significantly smaller than the applied magnetic field [13, 22].

In a recent study (Ref. [20]), both AC and static susceptibility measurements were conducted with a confocal microscope by demagnetizing the sample, elevating its temperature beyond its Curie point, and then assessing the stray fields. This approach allows to differentiate between the field emanating from the sample and the applied field. Alternatively, the utilization of NV^- center based quantum widefield diamond microscopes (QDM) [25, 26], offers another avenue to distinguish the applied field from the stray field of the sample. In a QDM, the magnetic field across a wide field of view (ranging from 10 micrometers to 1 millimeter) is mapped as in Ref. [13], with regions lacking magnetic material providing insights into the background or applied magnetic field. By subtracting the applied magnetic field, information regarding the stray magnetic field from the sample can be extracted. However, the application of continuous-wave optically detected magnetic resonance (ODMR) to sense magnetic fields from materials has been limited to low frequencies, typically in the range of several tens of kilohertz [27].

Here, we present a novel approach for measuring the AC susceptibility of permalloy (Py) micro-disks, each spanning micrometer dimensions, using QDM. We employ XY dynamical decoupling sequences in widefield [28, 29] to detect small AC magnetic fields emanating from the magnetic micro-disks at high frequencies. This technique allows us to discern changes in magnetic moment induced by the applied AC fields, which typically hover around $1\ \text{fJ T}^{-1}$, with a spatial resolution of approximately around $1\ \mu\text{m}$. Such precise measurements would pose significant challenges with conventional methodologies. Additionally, we delve into the implications of various non-idealities and imperfections that may influence the accuracy of these measurements.

* kasturis@ee.iitb.ac.in

[†] dshishir@iitb.ac.in

II. RESULTS AND DISCUSSION

A. Implementation

Figure 1(a) illustrates the experimental setup employed for measuring the DC, and the AC susceptibility of the micro-magnets. The Py micro-magnets are deposited on a 0.5 mm thick Lithium Niobate (LiNbO_3) substrate. The diameter of each micro-magnet is $5.8(4) \mu\text{m}$, and the thickness is 30 nm. The center-to-center distance between the micro-magnets is $25 \mu\text{m}$ as shown in Fig. 1(b). The substrate is placed on a 4 mm wide copper strip, which generates the AC excitation field (B_{AC}). The field from the copper strip is predominantly in the plane of the micro-magnets, along \hat{y} -axis, as depicted in Fig. 1(a). A current of 1 A through the strip-line generates a field of $100 \mu\text{T}$ along the NV^- axis. The static bias field (\vec{B}_{DC}) is established by a SmCo permanent magnet, oriented along one of the crystallographic axes of the NV^- center. The NV^- makes an angle of $\theta = 54.6^\circ$ relative to the surface normal of the diamond, in the $\hat{y} - \hat{z}$ plane as shown in Fig. 1(a). The static field can be adjusted within a range of 0.8 mT to 5 mT.

An optical excitation of 0.3 W at 532 nm is delivered through a 0.9 numerical aperture objective onto the diamond. The lateral dimensions of the diamond are $4 \text{ mm} \times 4 \text{ mm}$, and the thickness is 0.25 mm. The diamond features a $\{100\}$ front facet and $\langle 110 \rangle$ edge orientation, with a high isotopic purity of 99.99%, and a surface layer of 2 ppm ^{15}N , approximately $1 \mu\text{m}$ thick. The resulting red fluorescence is directed onto a high-speed lock-in camera after passing through requisite optical filters. The overall field of view spans $70 \mu\text{m} \times 70 \mu\text{m}$ with a each pixel being $1 \mu\text{m}$, and an overall magnification of 40. Further details are provided in Appendix. A.

B. Widefield DC Magnetometry

We first characterize the static properties of the micro-magnets by varying the external static field B_{DC} , and measuring the dipole moment of the micro-magnets. We derive the local magnetic field corresponding to each applied external magnetic field by examining the Zeeman splitting observed in the optically detected magnetic resonance (ODMR) signal from individual pixels of the camera. The Zeeman frequency encompasses contributions from both the applied external magnetic field, and the magnetic field generated by the micro-magnets. To differentiate the external magnetic field from the field of the micro-magnets, we first, filter the magnetic field image with a Gaussian filter which has a kernel size of 50 pixels. Subsequently, we subtract the filtered image from the original image, as outlined in [22] to obtain the field from the sample B_{DC}^s .

In Figure 2(a), we present the static magnetic field map from the sample when an external magnetic field of 1 mT is applied along the NV^- axis. The micro-magnets become magnetized, exhibiting a dipole moment of $107(5) \text{ fJT}^{-1}$. Analysis of the magnetic field map allows us to estimate the

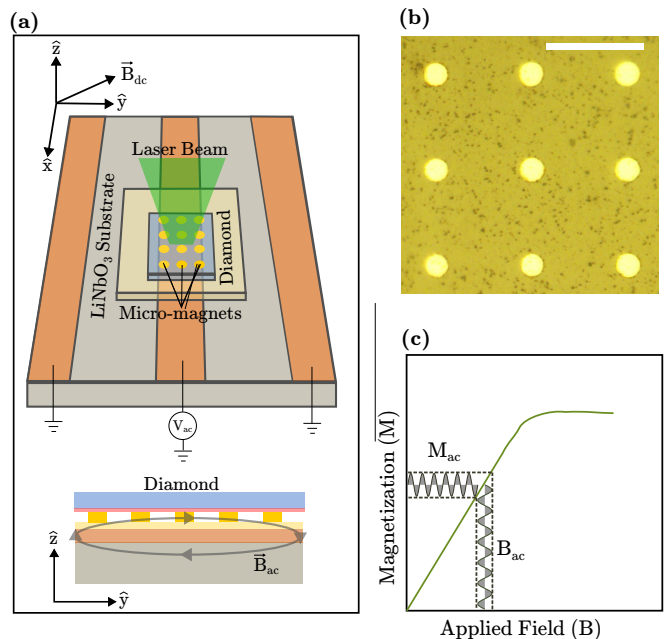


FIG. 1. Exepermental platform. (a). Permalloy micro-magnets of $5.8(4) \mu\text{m}$ diameter are patterned on a LiNbO_3 substrate. A permanent magnet is used to apply the static field B_{DC} along a NV^- axis. A 4 mm wide strip-line is used to provide the AC excitation B_{AC} . The AC field generated at the center of the strip-line is mostly along the \hat{y} -axis. Approximately $100 \mu\text{m}$ wide laser beam is used to excite the diamond. (b). Optical microscope image of the micro-magnets. The scale bar is $25 \mu\text{m}$. (c). To measure the AC susceptibility, an AC field B_{AC} is provided to the micro-magnets, which causes the magnetization of the micro-magnets to oscillate. The resultant oscillating stray field from the micro-magnets is measured by the NV^- centers in diamond.

offset distance between the NV^- layer and the micro-magnets to be approximately $6.0(7) \mu\text{m}$ (further details are provided in Appendix C). As the sample lacks perpendicular anisotropy, magnetization predominantly aligns within the plane due to the relatively large lateral dimensions compared to the thickness [8, 30]. The volume normalized magnetic susceptibility χ_V is defined as [8]

$$\chi_V = \frac{1}{V} \frac{\Delta m}{\Delta H_y}, \quad (1)$$

where Δm denotes the change in the dipole moment for a change in magnetic excitation ΔH_y . In our study, we adhere to SI units, where the magnetic dipole moment m is measured in JT^{-1} (equivalent to $1 \times 10^3 \text{ emu}$), the magnetic induction H is in A m^{-1} (1 A m^{-1} is equal to $4\pi \times 10^{-3} \text{ Oe}$), and the magnetic field $B = \mu_0 H$ is in T. In SI units, the volume-normalized susceptibility is a dimensionless quantity. Given that our magnetic field is aligned to a single axis of the NV^- center, we solely consider the in-plane magnetic field for calculating the susceptibility, denoted as H_y .

In Figures 2(b) to 2(d), we depict the stray field emanating from the central micro-magnet (circled in Fig. 2(a)) under excitation fields of 1 mT, 2 mT, and 3 mT, respectively.

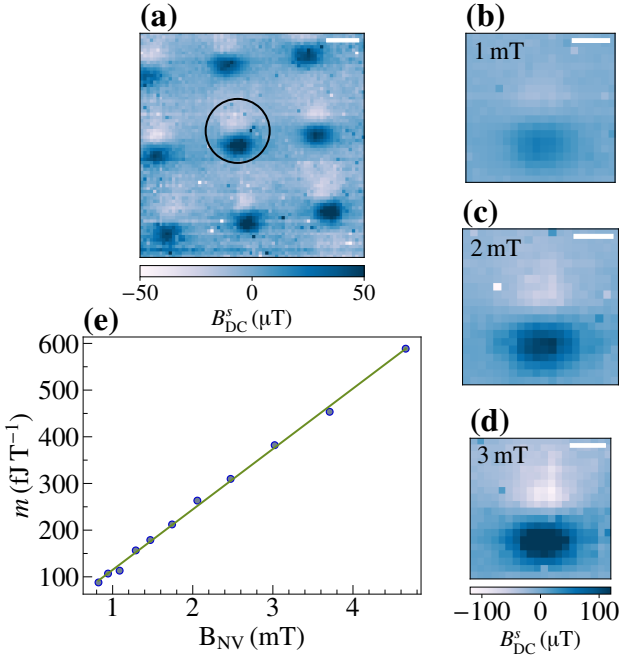


FIG. 2. Static micro-magnet characterization. (a). Static magnetic field from the micro-magnets when 1 mT field is applied along the NV^- axis. The scale bar is $10 \mu\text{m}$. (b). Static magnetic field from the central micro-magnet (circled in (a)) at 1 mT, (c) at 2 mT, and (d) at 3 mT. The scale bar for (b), (c), and (d) is $5 \mu\text{m}$. (e). Variation in dipole moment with applied magnetic field, fit to a straight line.

The stray field exhibits a direct proportionality to the magnetic dipole moment, evident in its escalation with increasing applied field strength. The extraction of the micro-magnets' dipole moment follows the procedure detailed in Appendix C.

The dipole moment demonstrates an almost linear increase at a rate of approximately $129 \text{ fJ T}^{-1} \text{ mT}^{-1}$, as illustrated in Figure 2(e). Extrapolation of the linear fit to zero magnetic field yields a small dipole moment of -14 fJ T^{-1} , indicating the absence of significant remnant magnetization, and suggesting a soft magnetic nature of the micro-magnets. Notably, the magnetic susceptibility for the central micro-magnet is measured to be $138(5)$ (the mean volume of each micro-magnet is $3.17 \mu\text{m}^3$), with similar values observed for the other micro-magnets.

C. Widefield AC Magnetometry

AC susceptometry on a magnetic sample is performed as shown in Fig. 1(c). An AC magnetic field of small amplitude is applied on top of a static magnetic field. The AC magnetic field results in the oscillation of sample's magnetization. The resultant AC stray field is measured by the NV^- centers. For performing widefield AC magnetometry, we use the XY-N dynamical decoupling sequences [20, 28, 31] (DD sequence). The exact pulse sequence is shown in Fig. 3(a). The pulse sequence consists of a train of π pulses sandwiched between two $\pi/2$ pulses with alternating x, y phases. The train of π pulses

rectifies the applied AC signal which results in a net phase Φ_{NV} acquired by the NV^- centers. The spacing τ between the π pulses is equal to half the period of the signal that is to be sensed, i.e. $\tau = 1/2f_{ac}$. The image acquisition is performed by Helios Helicam C3 lockin camera. Each demodulation cycle is divided into four parts namely - $I_1, Q_1, I_2,$ and Q_2 . After every demodulation cycle, the camera outputs two frames : $I_2 - I_1,$ and $Q_2 - Q_1$. In our experiment, the demodulation rate is 8 kHz. Hence, $I_1, Q_1, I_2,$ and Q_2 are each $31.25 \mu\text{s}$ long. We put the pulse sequence in $I_1, I_2,$ and the laser readout, and the polarization in $Q_1,$ and Q_2 . The pulse sequence in $I_1,$ and I_2 are essentially the same, but with $+x,$ and $-x$ final $\pi/2$ pulse respectively. Doing so, enhances the contrast of the signal [32]. To sense the response of the micro-magnets to an excitation frequency f_{ac} , we apply an AC excitation field whose component along the NV^- axis is given by

$$b_{AC}^a(t) = B_{AC}^a \cos(2\pi f_{ac}t + \delta), \quad (2)$$

where, f_{ac} is the excitation frequency, δ is the phase of the signal with respect to the initial $\pi/2$ pulse in the XY-N sequence. Note that the actual field is along the \hat{y} axis, and the component of the field along the NV^- axis is $\sqrt{2/3}$ times of it. The sample responds to the applied AC field with a field given by

$$b_{AC}^s(t) = B_{AC}^s \cos(2\pi f_{ac}t + \delta), \quad (3)$$

where we assume that there is no phase shift in the sample signal from the applied signal (see Appendix B for a more detailed analysis). In this case, the net phase acquired, Φ_{NV} , by the NV^- centers due to the DD sequence is given by [20, 31, 33]

$$\Phi_{NV} = 4\gamma_e N_p \tau B_{AC} \cos \delta = \kappa B_{AC} \cos \delta, \quad (4)$$

where N_p is the total number of π pulses, and γ_e is the electron gyro-magnetic ratio equal to $28.024 \text{ kHz } \mu\text{T}^{-1}$, and $B_{AC} = B_{AC}^a + B_{AC}^s$. The phase is converted to a fluorescence signal by the final $\pi/2$ pulse. The fluorescence signal is given by [20, 31, 33]

$$S_{XY} = C_o + C \cos(\Phi_{NV} \cos(\delta)), \quad (5)$$

where C is the contrast of the signal, and C_o is the baseline of the signal. Note that we are interested in extracting both the phase and the amplitude of the AC magnetic field. From Eq. (5), the sensitivity to the phase and the amplitude of the AC signal is given by

$$\frac{\partial S_{XY}}{\partial B_{AC}} = -C \cdot \kappa \cdot \sin(\kappa B_{AC} \cos \delta) \cos \delta \quad (6)$$

$$\frac{\partial S_{XY}}{\partial \delta} = C B_{AC} \cdot \kappa \cdot \sin(\kappa B_{AC} \cos \delta) \sin \delta. \quad (7)$$

From Eq. (6), it can be seen that the maximum sensitivity for detecting amplitude of the AC signal is achieved when the phase $\delta = 0$. However, at $\delta = 0$, the sensitivity to detect any change in phase is zero. From Eq. (7), a similar statement can be made about the sensitivity to detect the phase, which is maximum at $\delta = \pi/2$, at which the amplitude sensitivity is

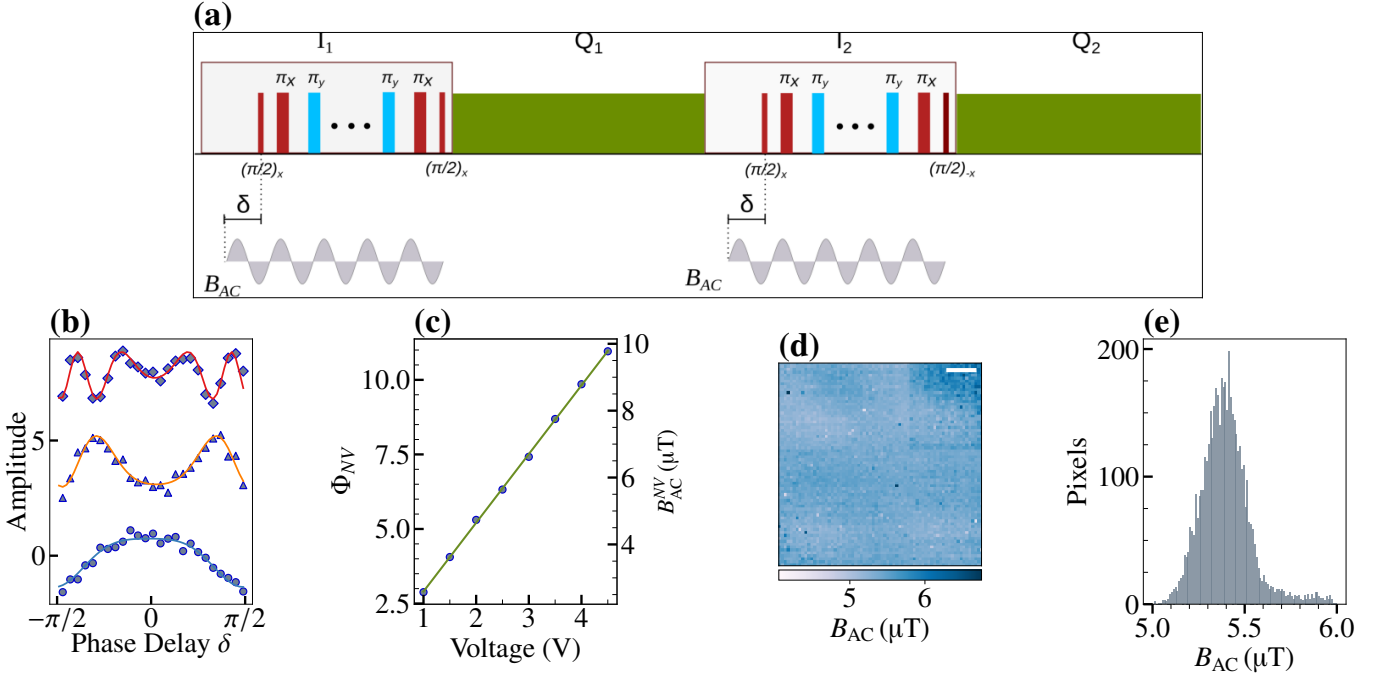


FIG. 3. Widefield AC magnetometry. (a). Pulse sequence used for widefield AC sensing. The pulse sequence consists of XY-N decoupling sequence. An external AC signal B_{AC} is provided through a current carrying strip. The initial phase δ of the external AC excitation with respect to the initial $\pi/2$ pulse is swept from $-\pi/2$ to $\pi/2$. (b). Signals resulting from the phase shift for an applied voltage of 1 V, 2 V, and 4 V fit to Eq. (5) at a random pixel. The pulse sequence used is the XY-4 sequence, and the AC signal frequency is 200 kHz. (c). The phase acquired by the NV^- center after the end of the sequence for various applied voltage fit to a straight line. (d). Widefield AC magnetic field map in the absence of micro-magnet sample. The scale-bar is $10 \mu\text{m}$. (e). Histogram of the detected AC magnetic field at an applied voltage of 3 V. The standard deviation across the pixels is 120 nT.

zero. Hence, we sweep the phase of the excitation signal of Eq. (2) from $\delta = 0$ to $\delta = \pi$ as Eq. (5) is periodic with π .

Initially, we examine the scenario where the micro-magnet sample is not present. In this instance, we utilize a LiNbO_3 substrate devoid of any micro-magnets, maintaining the same geometry as depicted in Fig. 1(a). To ascertain the durations of the π , and $\pi/2$ pulses, as well as the uniformity of the microwave drive strength, we conduct the widefield Rabi experiment. Due to the proximity of a neighboring hyperfine from a ^{15}N nucleus, we observe a composite of two sinusoidal waves. The data from a single pixel is fit to a sum of two exponentially decaying cosine functions [34]

$$A_1 \cos(\omega_1 t) e^{(-t/T_1)} + A_2 \cos(\omega_2 t) e^{(-t/T_2)}, \quad (8)$$

where ω_1 , and ω_2 are the Rabi frequencies. If, we assume, ω_1 is the slower frequency, corresponding to the resonant frequency, the faster frequency ω_2 is given by

$$\omega_2 = \sqrt{\omega_1^2 + \Delta^2}, \quad (9)$$

where Δ is the de-tuning from the resonance. In our experiment the mean value of ω_1 over all the pixels is $2\pi \times 2.7 \text{ Mrad s}^{-1}$, and the mean value of ω_2 over all the pixels is $2\pi \times 4 \text{ Mrad s}^{-1}$. Using Eq. (9), we find that Δ is equal to $2\pi \times 3 \text{ Mrad s}^{-1}$, which is approximately equal to the hyperfine frequency of the ^{15}N spin. In the absence of a sample,

the variation π pulse times is less than 6 ns, indicating a high degree of uniformity. In Fig. 3(b), the signal obtained from a random pixel, for various applied voltages is shown at a frequency of 200 kHz using a XY-4 $((\pi/2)_x - \tau/2 - \pi_x - \tau - \pi_y - \tau - \pi_x - \tau - \pi_y - \tau/2 - (\pi/2)_x)$ decoupling sequence. The signals follow the functional relationship given in Eq. (5). By fitting the equation, we obtain a linear relationship between the applied voltage and the phase Φ_{NV} , acquired by the NV^- centers as shown in Fig. 3(c). The applied AC field is proportional to the phase acquired by the NV^- centers Φ_{NV} as given Eq. (4). The resulting widefield image is shown in Fig. 3(d). The AC field histogram across various pixels is shown in Fig. 3(e). The standard deviation of the sensed AC magnetic field is 120 nT.

A significant challenge encountered when sensing AC fields from magnetic materials using dynamical decoupling sequences is the impact of DC inhomogeneities [22, 35, 36]. The static magnetic field emanating from these materials can induce de-tuning effects on the applied π and $\pi/2$ pulses. Since a de-tuned microwave signal fails to induce a complete transition from $|0\rangle$ to $|1\rangle$, errors may arise in the sensed field. To assess the errors stemming from these inhomogeneities, we initially simulate their effects. In this work, we measure the initial AC susceptibility, when an external static magnetic field of 0.8 mT is applied along the NV^- axis. In Fig. 4(a), we present the experimentally obtained Rabi frequency map around the central micro-magnet under an applied static magnetic field of 0.8 mT along the NV^- axis. The nominal Rabi

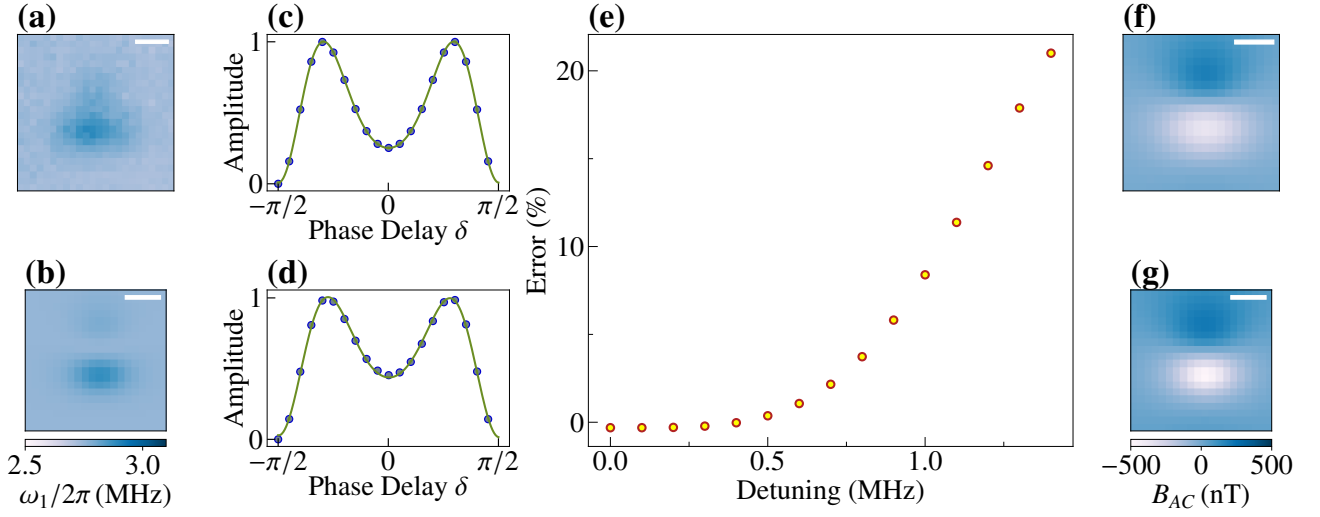


FIG. 4. Effects of inhomogeneity. (a). Experimentally obtained variation of Rabi frequency around a micro-magnet. The Rabi frequency away from the micro-magnet is 2.7 MHz. At the location of maximum field from the micro-magnet, the Rabi frequency is 2.85 MHz. (b). Simulated Rabi frequency for a micro-magnet. (c). Simulated XY-8 signal for an applied AC field of $3.5 \mu\text{T}$ without any de-tuning. (d). Simulated XY-8 signal for an applied AC field of $3.5 \mu\text{T}$ for a de-tuning of 0.9 MHz. Note the resulting signal sensed AC signal is less than the applied AC signal in this case. (e). Percentage error in the sensed AC signal for various de-tunings. The base Rabi frequency is assumed to be 2.7 MHz. (f). Simulated AC field from a micro-magnet in the absence of in-homogeneities. (g). Simulated AC field from a micro-magnet in the presence of in-homogeneities. The scale-bar in all the figures is $5 \mu\text{m}$.

frequency hovers around 2.7 MHz, yet due to the de-tuning induced by the micro-magnet's field, the Rabi frequency escalates to 2.85 MHz at the micro-magnet's maximal field point. This increase in Rabi frequency, corresponding to a de-tuning of approximately 0.9 MHz, as can be deduced from Eq. (9).

In Fig. 4(b), we present the corresponding simulated Rabi frequency map for a micro-magnet. To comprehend the impact of de-tuning on the sensed magnetic field, we compute the phase acquired as a function of phase shift δ under conditions of perfect and imperfect π pulses. Fig. 4(c) displays the simulated signal for perfect π and $\pi/2$ pulses under an applied AC magnetic field of $3.5 \mu\text{T}$, and a frequency of 300 kHz. As anticipated, fitting to Eq. (5) yields the expected $3.5 \mu\text{T}$. However, with an applied de-tuning of 0.9 MHz, the acquired net phase diminishes, resulting in an erroneously sensed AC signal of $3.25 \mu\text{T}$. This discrepancy arises from the imperfect nature of the π and $\pi/2$ pulses, which only elevate the NV^- centers to $0.9|1\rangle$ instead of the excited state $|1\rangle$. Regardless of whether the signal is de-tuned to the right or left, the net sensed signal is consistently less than the applied signal, as depicted in Fig. 4(d) [36]. This observation aligns with Eq. (9). In Fig. 4(e), we illustrate the error in the sensed signal due to imperfect pulses. Notably, negligible error is evident until approximately 0.5 MHz, beyond which the error escalates significantly, reaching nearly 20% for a de-tuning of 2 MHz. It's worth noting that the error consistently manifests negatively, indicating that the sensed field is consistently underestimated compared to the actual applied field. Fig. 4(f) presents the AC simulated magnetic field map from a micro-magnet, while Fig. 4(g) illustrates the sensed magnetic field map due to π pulse errors. The positive lobe of the field remains mostly unaffected since most de-tuning in this region is

below 0.5 MHz. However, certain parts of the negative lobe exhibit more negative values than actual. Nevertheless, the slope of the line connecting the negative lobe and the positive lobe remains nearly constant, serving as the basis for estimating the change in dipole moment due to applied AC excitation (refer to Appendix C). Another imperfection may arise from the background AC magnetic field originating from the static magnetization of the micro-magnet. The off-axis DC field from the micro-magnet can generate an AC field proportional to the micro-magnet's magnetization. The AC magnetic field acquired due to such off-axis field is given by [20]

$$\tilde{B}_\perp = \frac{3\gamma_e}{D_o} (B_{NV\perp} \times \tilde{B}_{NV\perp}), \quad (10)$$

where $B_{NV\perp}$ is static perpendicular magnetic field, and $\tilde{B}_{NV\perp}$ is the AC perpendicular magnetic field. In our case, $\tilde{B}_{NV\perp}$ is around $2 \mu\text{T}$, and $B_{NV\perp}$ is around $40 \mu\text{T}$. Substituting these values into equation Eq. (10), we get a field \tilde{B}_\perp of around 2 nT, which is far lower than the AC field from the micro-magnet and hence we can neglect it.

Fig. 5(a) displays the resultant AC magnetic field map for an excitation of $3.5 \mu\text{T}$ at a frequency of 300 kHz. In our experiments, we employ the XY-4 sequence for excitation frequencies of 200 kHz and 250 kHz, while adopting the XY-8 sequence for higher frequencies. The field map depicted in Fig. 5(a), and subsequent maps have had the effect of the excitation field removed. Fig. 5(b) zooms in on the AC magnetic field from the central micro-magnet. Both positive and negative lobes are clearly discernible, indicating that the field map is not solely a result of DC de-tuning but rather represents an actual AC magnetic field emanating from the micromagnet. Fig. 5(c) to Fig. 5(e) illustrate the contrast variation as a func-

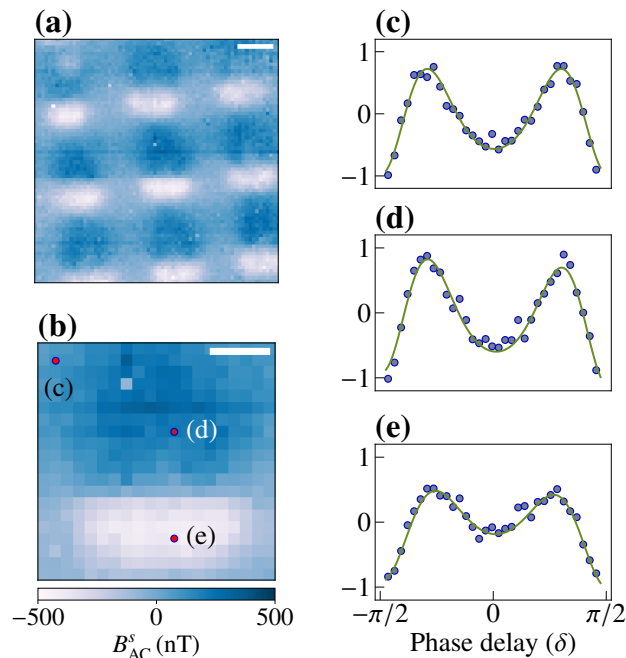


FIG. 5. AC magnetic field from micro-magnets. (a). Wide-field image of AC magnetic field image from the micro-magnets. The micro-magnets were excited with a field of amplitude $3.5 \mu\text{T}$ and a frequency of 300 kHz . The sensing is done using the XY-8 DD sequence. The image is acquired by averaging three datasets each acquired for a time duration of 15 min. The scale-bar is $10 \mu\text{m}$. (b). Zoomed in image of the central micro-magnet. The scale-bar is $5 \mu\text{m}$. (c), (d), (e) The XY-8 phase delay signal at pixels labeled (c), (d), and (e) in (b) fit to Eq. (5).

tion of phase delay δ , fitted to Eq. (5) for points labeled in Fig. 5(b).

In Fig. 6(a), the volume-normalized susceptibility χ_V is depicted for various applied frequencies of up to 500 kHz . It's noteworthy that χ_V closely mirrors the DC susceptibility across this frequency range due to the rapid movement of domain walls in Py, facilitating the magnetization's quick alignment with the applied magnetic field within a very short period of time compared to the period of the excitation signal. An essential aspect of AC susceptibility measurements is considering the phase of the sample's signal with respect to the excitation field. When the AC excitation period is similar to the relaxation time of the magnetic material, the magnetization lags behind the magnetic excitation. Assuming the magnetization response adheres to a damped harmonic oscillator model, nearing resonance with the AC excitation frequency results in a reduction of the in-phase component of magnetization, leaving predominantly the out-of-phase component. Consequently, the field emitted by the micro-magnet undergoes a 90° phase shift with respect to the excitation signal.

Fig. 6(b) illustrates the phase variation surrounding a micro-magnet at an excitation frequency of 300 kHz . The majority of pixels in the vicinity of the micro-magnet display phase fluctuations ranging from 1° to 2° , indicating that noise is the primary contributor to this minor fluctuation. This presented phase reflects the overall signal phase with respect

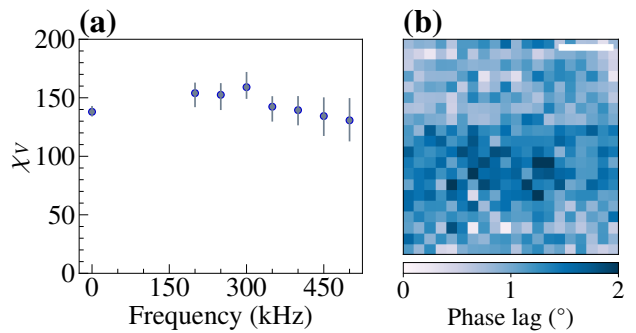


FIG. 6. AC susceptibility. (a). Real part of the AC susceptibility at various frequencies. (b). Phase relative to the excitation signal around the central micro-magnet at $3.5 \mu\text{T}$ excitation and 300 kHz frequency. The scale-bar is $5 \mu\text{m}$.

to the XY-N sequence. Given that the overall signal phase demonstrates no notable deviation from the XY-N signal, we infer that the micro-magnet's field similarly exhibits negligible phase shifts (see Appendix B for additional analysis).

III. CONCLUSION AND OUTLOOK

In summary, our study successfully demonstrated the measurement of micro-scale AC susceptibility utilizing NV^- centers in diamond within a widefield configuration employing the XY dynamical decoupling sequences. Through the excitation of micro-magnets with AC magnetic fields, we were able to detect the stray field emanating from these micro-magnets, corresponding to a change of approximately 1 fJ T^{-1} of magnetic moment. Moreover, leveraging our pixel resolution of $1 \mu\text{m}$ and a field of view spanning $70 \mu\text{m}$, we effectively mapped the AC susceptibility across an array of 9 micro-magnets spaced at intervals of $25 \mu\text{m}$. Additionally, our methodology facilitated the measurement of the phase of the magnetic field originating from the micro-magnets, thanks to the phase-sensitive sensing protocol. Furthermore, we conducted an analysis to identify sources of non-idealities, pinpointing static inhomogeneity as a significant factor. This static inhomogeneity contributes to errors in the π pulses within the sensing protocol, underscoring the importance of addressing such challenges for enhanced accuracy in future measurements.

ACKNOWLEDGEMENT

K.S. acknowledges financial support from DST Quest, SERB Power Research Grant, AOARD grant FA2386-23-1-4012 and I-Hub Divya Sampark Grant in addition to support from IITB Nano-Fabrication facility for sample preparation.

CONFLICT OF INTEREST

The authors have no conflicts to disclose.

DATA AVAILABILITY

The data that support the findings of this work is available upon reasonable request from the authors.

Appendix A: Experimental Setup

We use a home built widefield microscope for the experiments. The diamond used is a square of side 4 mm, and thickness 250 μm , and is provided by Element six. The inherent T_2 of the diamond measured using an XY-8 pulse sequence is 21 μs . Hence, we keep the length of our sequence near this value. For example, the length of an XY-8 sequence for sensing a frequency of 300 kHz signal, including micro-wave pulses, is 14.8 μs . Moreover, the minimum frame rate of the camera is 2.5 kHz. This restriction demands the length of the sequence to be less than 100 μs .

The diamond is excited by 532 nm diode laser (Sprout H) via a 100x, 0.9 NA objective (Olympus MPlanFL N), and the resultant fluorescence is collected through the same objective. The incident laser power is 300 mW. The red fluorescence collected passes through band pass filters (690 nm to 800 nm) and is recorded by the lockin camera (Heliotis C3). The camera records at a frame rate 8 kHz. The microwave signals are provided by a microwave signal generator (SRS386), and amplified by an amplifier (Mini-Circuits ZHL-16W-43-S+). DC to microwave switches (Mini-Circuits ZASWA-2-50DR+) are used to switch the micro-waves as well as to provide switching for the IQ modulation. The phases of the pulses are controlled by the in-built IQ modulation of the signal generator, as described in [29]. The AC excitation is provided by a 4 mm wide copper strip which is terminated by two 3 Ω , and 1 W rated resistors using a function generator (Tectronix AFG1022). The pulses are provided by Pulseblaster ESRPro500 pulse generator.

The permalloy samples were prepared by patterning 7 μm diameter disks on LiNbO_3 substrate using photolithography, and then sputtering a stack of $\text{Ti}/\text{Ni}_{0.8}\text{Fe}_{0.2}/\text{Pt}$ (5 nm/30 nm/10 nm) on it. However, after deposition, we found the diameter of the micro-magnets to have shrunken to 5.8(4) μT . We used LiNbO_3 as the substrate because it is an insulating material. We found that any conducting surface near the NV^- layer degrades the micro-wave power, in-turn, reducing the Rabi oscillation frequency.

Appendix B: Magnitude and Phase Sensitivity

The magnitude and phase sensitivity can be derived from Eq. (6), and Eq. (7). The minimum magnitude of AC field that

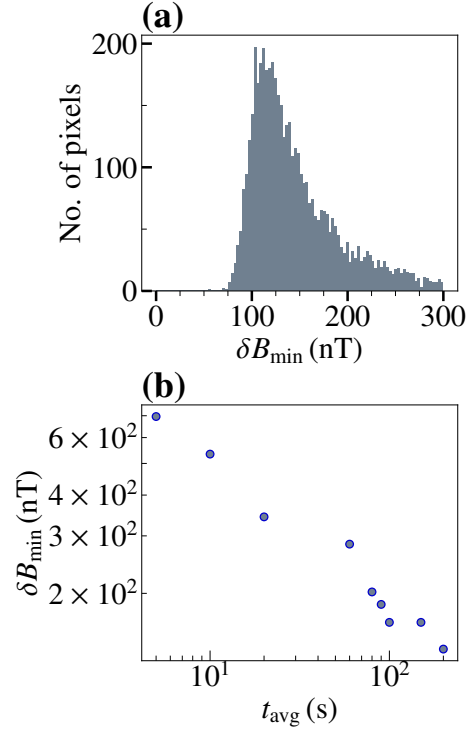


FIG. 7. Magnitude and phase sensitivity. (a). Histogram of the number of minimum detectable magnetic field δB_{\min} defined in Eq. (B1) across the pixels for an averaging time of 200 s. (b). Dependence of median minimum detectable signal with averaging time t_{avg} .

can be sensed is given by

$$\Delta B_{\text{AC}}^{\min} = \frac{\sigma_{S_{XY}}}{\left| \frac{\partial S_{XY}}{\partial B_{\text{AC}}} \right|_{\max}} = \frac{\sigma_{S_{XY}}}{C\kappa} \quad (\text{B1})$$

where $\sigma_{S_{XY}}$ is the standard deviation in the XY signal for a fixed initial phase. From Eq. (6), it can be seen that the maximum slope occurs when the initial phase $\delta = 0$, and $\kappa B_{\text{AC}} = (2n + 1)\pi/2$. In Fig. 7(a), the histogram of the minimum detectable field as defined in Eq. (B1) for an applied AC magnetic field of 5 μT and an acquisition time of 200 s is shown. The median value of ΔB_{\min} is 135 nT, with around 80% of the pixels lying between 75 nT to 180 nT. Moreover, for an averaging time of 5 s, the median minimum detectable field is 630 nT as shown in Fig. 7(b).

The phase sensitivity, as can be seen from Eq. (7), is intricately connected to the amplitude of the AC field B_{AC} . The minimum phase that can be detected around $\delta = (2n + 1)\pi/2$ is given by

$$\Delta \delta_{\min} = \frac{\sigma_{S_{XY}}}{\left| \frac{\partial S_{XY}}{\partial B_{\text{AC}}} \right|_{\max}} = \frac{\sigma_{S_{XY}}}{C \cdot B_{\text{AC}} \cdot \kappa}. \quad (\text{B2})$$

The equation for minimum detectable phase as can be seen from Eq. (B2) is similar to the the equation for minimum detectable magnitude in Eq. (B1), but with a scaling factor of B_{AC} . Thus, for 200 s averaging, and an applied excitation of 5 μs , the minimum detectable phase of around 1.6 $^\circ$.

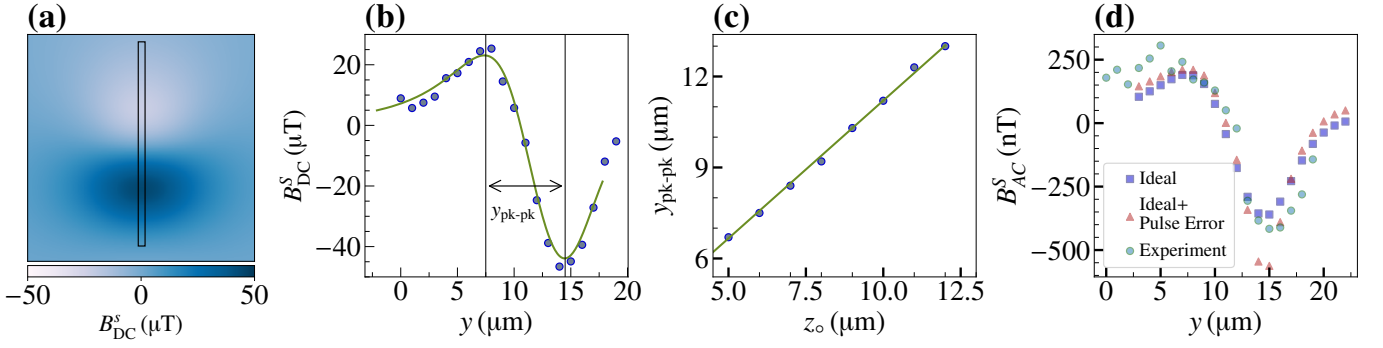


FIG. 8. (a). Calculated stray magnetic field for a micro-magnet at a stand-off distance of $5.5 \mu\text{m}$. The rectangular box indicates the line-cut at 1 mT applied field (See Fig. 2(b) for experimental map). (b). Line cut along the dipole. The data points are from the experiment magnetic field map in Fig. 2(b). (c). Peak to peak distance $y_{\text{pk-pk}}$ as a function of stand-off distance z_0 fit to a straight line. (d). The blue dots represent line cut of the simulated AC field from the sample (see Fig. 4(f)). The green dots represent the line cut from Fig. 5(b), and finally the orange dots represent the line cut from Fig. 4(g).

However, an important point to note here is that in the case of AC susceptibility, we are mainly interested in measuring the phase of the field from the micro-magnets with respect to the excitation field *rather than* the phase of the total AC signal with respect to the first $\pi/2$ pulse. Let us consider the case where, due to the excitation given in Eq. (2), the field from the sample is

$$b_{\text{AC}}^s(t) = B_{\text{AC}}^s \cos(2\pi f_{\text{ac}}t + \delta + \delta_s), \quad (\text{B3})$$

then the total field B_{AC} will experience an additional phase shift δ_{add} from δ that is equal to

$$\tan \delta_{\text{add}} = \frac{B_{\text{AC}}^s \sin \delta_s}{B_{\text{AC}}^a + B_{\text{AC}}^s \cos \delta_s}. \quad (\text{B4})$$

For a case where $B_{\text{AC}}^a \gg B_{\text{AC}}^s$, and a shift in-phase that is close to zero, we get a relationship

$$\delta_{\text{add}} = \frac{B_{\text{AC}}^s}{B_{\text{AC}}^a} \delta_s. \quad (\text{B5})$$

Combining Eq. (B5), and Eq. (B2), we get

$$\Delta \delta_s^{\text{min}} = \frac{\sigma_{S_{\text{XY}}}}{C \cdot B_{\text{AC}}^s \cdot k}. \quad (\text{B6})$$

In our case the maximum field from the micro-magnet is around 10 times smaller than the excitation field. The minimum detectable phase in this case would be 16° . However, because, the AC field from the micro-magnet is not uniform, the minimum detectable phase would also not be uniform. Another case of significant importance is the case where $\delta_s \rightarrow \pi/2$. In such a case, using Taylor expansion around $\pi/2$, and ignoring quadratic terms, we get from Eq. (B4) the net phase acquired is

$$\delta_{\text{add}} = \frac{B_{\text{AC}}^s}{B_{\text{AC}}^a}. \quad (\text{B7})$$

For a perspective if $B_{\text{AC}}^s/B_{\text{AC}}^a = 1/10$, a phase shift of 90° from the sample signal will result in a phase shift of 5.7° in the total signal.

Appendix C: Micro-magnet Model

The formulas to calculate the stray magnetic field from a cylindrical magnet of arbitrary uniform magnetization are provided in Ref. [37]. We use these formulas to extract the dipole moment of the micro-magnet from the stray magnetic-field. First, we calculate the stray magnetic field profile of a $5.8 \mu\text{m}$ diameter micro-magnet of a given dipole moment for various stand-off distances. The projection of the stray magnetic field along the NV^- axis is given by $B_{\text{NV}} = \sqrt{2/3} B_y + \sqrt{1/3} B_z$ [38]. The peak-to-peak distance on the line-cut along the center of the field map is indicative of the stand-off distance, and the slope of the line joining the peak-to-peak is directly proportional to the magnitude of dipole moment. In Fig. 8(a), the calculated magnetic field map for a cylinder along an NV^- axis for a dipole moment of 107 fJ T^{-1} , and a stand-off distance of $6 \mu\text{m}$ is shown. The line-cut is shown in Fig. 8(b) with the experimental data from Fig. 2(c). In Fig. 8(c), the peak-to-peak distance is plotted against the stand-off distance. For a point sized dipole object, the stand-off distance would be equal to the peak-to-peak distance. However, in the case of an extended dipole, the relationship would not be perfectly linear. We obtain the following linear fit for the relationship between the peak-to-peak distance and the stand-off distance

$$y_{\text{pk-pk}} = 2.12 + 0.9z_0, \quad (\text{C1})$$

where $y_{\text{pk-pk}} (\mu\text{m})$ is the peak-to-peak distance, and $z_0 (\mu\text{m})$ is the stand-off distance. The slope increases by $14.3 \mu\text{T} \mu\text{m}^{-1}$ for an increase in the dipole moment of 100 fJ T^{-1} , at the previously stated stand-off distance. In Fig. 8(d), the line cuts for AC fields from the micro-magnets is shown for a frequency of 300 kHz. The experimental data fits well with the ideal simulated data, and does not show a pronounced peak at the negative lobe as predicted by the error in the de-tuning. However, as can be seen, the slope of all the three lines is very close to each other.

- [1] L. Ramasubramanian, A. Kákay, C. Fowley, O. Yildirim, P. Matthes, S. Sorokin, A. Titova, D. Hilliard, R. Böttger, R. Hübner, S. Gemming, S. E. Schulz, F. Kronast, D. Makarov, J. Fassbender, and A. Deac, *ACS Applied Materials & Interfaces* **12**, 27812 (2020).
- [2] T. Shinjo, T. Okuno, R. Hassdorf, K. Shigeto, and T. Ono, *Science* **289**, 930 (2000), <https://www.science.org/doi/pdf/10.1126/science.289.5481.930>.
- [3] D. D. Stueber, J. Villanova, I. Aponte, Z. Xiao, and V. L. Colvin, *Pharmaceutics* **13** (2021), 10.3390/pharmaceutics13070943.
- [4] I.-M. Hsing, Y. Xu, and W. Zhao, *Electroanalysis* **19**, 755 (2007).
- [5] K. S. Burch, D. Mandrus, and J.-G. Park, *Nature* **563**, 47 (2018).
- [6] A. Hirohata, K. Yamada, Y. Nakatani, I.-L. Prejbeanu, B. Diény, P. Pirro, and B. Hillebrands, *Journal of Magnetism and Magnetic Materials* **509**, 166711 (2020).
- [7] C. V. Topping and S. J. Blundell, *Journal of Physics: Condensed Matter* **31**, 013001 (2018).
- [8] B. D. Cullity and C. D. Graham, *Introduction to magnetic materials* (John Wiley & Sons, 2011).
- [9] L. Postulka, P. Eibisch, A. Holzmann, B. Wolf, and M. Lang, *Review of Scientific Instruments* **90**, 033901 (2019).
- [10] L. Toraille, K. Aizel, É. Balloul, C. Vicario, C. Monzel, M. Coppey, E. Secret, J.-M. Siaugue, J. Sampaio, S. Rohart, N. Vernier, L. Bonnemay, T. Debuisschert, L. Rondin, J.-F. Roch, and M. Dahan, *Nano Letters* **18**, 7635 (2018).
- [11] B. J. Maertz, A. P. Wijnheijmer, G. D. Fuchs, M. E. Nowakowski, and D. D. Awschalom, *Applied Physics Letters* **96**, 092504 (2010), https://pubs.aip.org/aip/apl/article-pdf/doi/10.1063/1.3337096/14426413/092504.1_online.pdf.
- [12] S. Hsieh, P. Bhattacharyya, C. Zu, T. Mittiga, T. J. Smart, F. Machado, B. Kobrin, T. O. Höhn, N. Z. Rui, M. Kamrani, S. Chatterjee, S. Choi, M. Zalelet, V. V. Struzhkin, J. E. Moore, V. I. Levitas, R. Jeanloz, and N. Y. Yao, *Science* **366**, 1349 (2019), <https://www.science.org/doi/pdf/10.1126/science.aaw4352>.
- [13] S. Dasika, M. Parashar, and K. Saha, *Review of Scientific Instruments* **94**, 053702 (2023), <https://pubs.aip.org/aip/rsi/article-pdf/doi/10.1063/5.0138301/17148139/053702.1.5.0138301.pdf>.
- [14] J.-P. Tetienne, T. Hingant, L. Rondin, S. Rohart, A. Thiaville, J.-F. Roch, and V. Jacques, *Phys. Rev. B* **88**, 214408 (2013).
- [15] M. Huang, J. C. Green, J. Zhou, V. Williams, S. Li, H. Lu, D. Djugba, H. Wang, B. Flebus, N. Ni, and C. R. Du, *Nano Letters* **23**, 8099 (2023).
- [16] D. A. Broadway, S. C. Scholten, C. Tan, N. Dontschuk, S. E. Lillie, B. C. Johnson, G. Zheng, Z. Wang, A. R. Oganov, S. Tian, C. Li, H. Lei, L. Wang, L. C. L. Hollenberg, and J.-P. Tetienne, *Advanced Materials* **32**, 2003314 (2020), <https://onlinelibrary.wiley.com/doi/pdf/10.1002/adma.202003314>.
- [17] F. Meneses, R. Qi, A. J. Healey, Y. You, I. O. Robertson, S. C. Scholten, A. Keerthi, G. Harrison, A. Bera, H. Jyothilal, L. C. L. Hollenberg, B. Radha, and J.-P. Tetienne, *Phys. Rev. B* **109**, 064416 (2024).
- [18] A. J. Healey, S. Rahman, S. C. Scholten, I. O. Robertson, G. J. Abrahams, N. Dontschuk, B. Liu, L. C. L. Hollenberg, Y. Lu, and J.-P. Tetienne, *ACS Nano* **16**, 12580 (2022).
- [19] A. Laraoui and K. Ambal, *Applied Physics Letters* **121**, 060502 (2022), https://pubs.aip.org/aip/apl/article-pdf/doi/10.1063/5.0091931/16480572/060502.1_online.pdf.
- [20] X.-Y. Zhang, Y.-X. Wang, T. A. Tartaglia, T. Ding, M. J. Gray, K. S. Burch, F. Tafti, and B. B. Zhou, *PRX Quantum* **2**, 030352 (2021).
- [21] I. O. Robertson, C. Tan, S. C. Scholten, A. J. Healey, G. J. Abrahams, G. Zheng, A. Manchon, L. Wang, and J.-P. Tetienne, *2D Materials* **10**, 015023 (2022).
- [22] R. W. de Gille, J. M. McCoe, L. T. Hall, J.-P. Tetienne, E. P. Malkemper, D. A. Keays, L. C. L. Hollenberg, and D. A. Simpson, *Proceedings of the National Academy of Sciences* **118**, e2112749118 (2021), <https://www.pnas.org/doi/pdf/10.1073/pnas.2112749118>.
- [23] F. Xu, S. Zhang, L. Ma, Y. Hou, J. Li, A. Denisenko, Z. Li, J. Spatz, J. Wrachtrup, H. Lei, Y. Cao, Q. Wei, and Z. Chu, *Science Advances* **10**, eadi5300 (2024), <https://www.science.org/doi/pdf/10.1126/sciadv.adi5300>.
- [24] M. Kayci, J. Fan, O. Bakirman, and A. Herrmann, *Proceedings of the National Academy of Sciences* **118**, e2112664118 (2021), <https://www.pnas.org/doi/pdf/10.1073/pnas.2112664118>.
- [25] M. Parashar, A. Bathla, D. Shishir, A. Gokhale, S. Bandyopadhyay, and K. Saha, *Scientific Reports* **12**, 8743 (2022).
- [26] E. V. Levine, M. J. Turner, P. Kehayias, C. A. Hart, N. Langellier, R. Trubko, D. R. Glenn, R. R. Fu, and R. L. Walsworth, *Nanophotonics* **8**, 1945 (2019).
- [27] R. S. Schoenfeld and W. Harneit, *Phys. Rev. Lett.* **106**, 030802 (2011).
- [28] Z. Wang, C. McPherson, R. Kadado, N. Brandt, S. Edwards, W. Casey, and N. Curro, *Phys. Rev. Appl.* **16**, 054014 (2021).
- [29] D. B. Bucher, D. P. L. Aude Craik, M. P. Backlund, M. J. Turner, O. Ben Dor, D. R. Glenn, and R. L. Walsworth, *Nature Protocols* **14**, 2707 (2019).
- [30] K. Roy, S. Bandyopadhyay, and J. Atulasimha, *Applied Physics Letters* **99**, 063108 (2011), https://pubs.aip.org/aip/apl/article-pdf/doi/10.1063/1.3624900/14456471/063108.1_online.pdf.
- [31] C. L. Degen, F. Reinhard, and P. Cappellaro, *Rev. Mod. Phys.* **89**, 035002 (2017).
- [32] C. A. Hart, J. M. Schloss, M. J. Turner, P. J. Scheidegger, E. Bauch, and R. L. Walsworth, *Phys. Rev. Appl.* **15**, 044020 (2021).
- [33] K. Mizuno, H. Ishiwata, Y. Masuyama, T. Iwasaki, and M. Hatano, *Scientific Reports* **10**, 11611 (2020).
- [34] Y. Yang, H. H. Vallabhapurapu, V. K. Sewani, M. Isarov, H. R. Firgau, C. Adambukulam, B. C. Johnson, J. J. Pla, and A. Laucht, *American Journal of Physics* **90**, 550 (2022), https://pubs.aip.org/aapt/ajp/article-pdf/90/7/550/19799837/550.1_online.pdf.
- [35] J.-P. Tetienne, D. A. Broadway, S. E. Lillie, N. Dontschuk, T. Teraji, L. T. Hall, A. Stacey, D. A. Simpson, and L. C. L. Hollenberg, *Sensors* **18** (2018), 10.3390/s18041290.
- [36] J. E. Lang, T. Madhavan, J.-P. Tetienne, D. A. Broadway, L. T. Hall, T. Teraji, T. S. Monteiro, A. Stacey, and L. C. L. Hollenberg, *Phys. Rev. A* **99**, 012110 (2019).
- [37] A. Caciagli, R. J. Baars, A. P. Philippe, and B. W. Kuipers, *Journal of Magnetism and Magnetic Materials* **456**, 423 (2018).
- [38] J. M. Schloss, J. F. Barry, M. J. Turner, and R. L. Walsworth, *Phys. Rev. Appl.* **10**, 034044 (2018).